



Cellulose Nanofibers-Polyacrylamide Hydrogel Based on Co-Electrolyte System for Solid-State Zinc Ion Batteries to Operate at Extremely Cold Temperatures

Journal:	<i>Journal of Materials Chemistry A</i>
Manuscript ID	TA-ART-09-2021-008023.R1
Article Type:	Paper
Date Submitted by the Author:	15-Oct-2021
Complete List of Authors:	Xu, Wangwang; Louisiana State University, Mechanical Engineering Liu, Chaozheng; Nanjing Forestry University, Ren, Suxia; Henan Key Laboratory of Biomass Energy, Lee, Danbee; Louisiana State University Gwon, Jae-Gyoung; Korea Forest Research Institute, Forest Products Flake, John; Louisiana State University, Chemical Engineering Lei, Tingzhou; Henan Academy of Sciences, Baisakh, Niranjana; Louisiana State University Wu, Qinglin; Louisiana State University System, ;

Cellulose Nanofiber-Polyacrylamide Hydrogel Based on Co-Electrolyte System for Solid-State Zinc Ion Batteries to Operate at Extremely Cold Temperatures

*Wangwang Xu, Chaozheng Liu, Suxia Ren, Danbee, Lee, Jaegyoun Gwon, John C. Flake, Tingzhou Lei, Niranjana Baisakh, and Qinglin Wu**

Dr. W. Xu, Prof. Q. Wu, Mr. Danbee Lee
School of Renewable Natural Resources, Louisiana State University Agricultural Center,
Baton Rouge, 70803, USA
E-mail: wxu26@lsu.edu; wuqing@lsu.edu

Dr. C. Liu,
Co-Innovation Center of Efficient Processing and Utilization of Forest Resources, College of
Materials Science and Engineering, Nanjing Forestry University, Nanjing, 210000, China

Dr. S. Ren, Dr. T. Lei
Institute of Urban & Rural Mining CCZU, Changzhou University, Changzhou 213164, China

Dr. Jaegyoun Gwon, Forest products department, National institute of Forest Science, 57
Hoegiro, Dongdaemun-gu, Seoul 02455

Prof. John C. Flake
Cain Department of Chemical Engineering, Louisiana State University AgCenter, Baton
Rouge, LA 70803, United States

Prof. Niranjana Baisakh
School of Plant, Environmental and Soil Sciences, Louisiana State University Agcenter,
Baton Rouge, LA 70803, United States

Keywords: CNF-PAM hydrogel electrolyte; methanol and water hybrid electrolyte; eutectic point; high reversibility of zinc anode; flexible solid-state zinc-ion battery

Solid-state zinc batteries (ssBs) based on hydrogel electrolyte have received a tremendous attention due to their reliable safety, high flexibility and robust performance. However, freezing of hydrogel electrolyte and resulted low ionic conductivity limit the capability of the ssBs to work at low temperatures. Herein, wood based cellulose nanofiber (CNF)-polyacrylamide (PAM) hydrogel electrolyte was developed with a hybrid methanol/water solvent. At the optimized methanol molar ratio of 56% (Me56), the hybrid electrolyte shows low freezing point and high-Zn²⁺ reversibility. The reversibility of Zn anode is boosted in this antisolvent since the Zn²⁺ solvation is weakened and corrosion reactions is suppressed. With the Me56 hybrid electrolyte, the MgVO/Zn batteries can deliver a high specific capacity of 214 mAh/g after 4000 cycles at 10 A/g (charging time: about 1 minute). The developed CNF-PAM hydrogel maintains high flexibility under repeated bending and twisting at very cold conditions. At the extremely low temperature of -60 °C, the ssBs still deliver a high specific capacity of about 140 mAh/g at 10 mA/g while remaining flexible, exhibiting a great potential to be applied in wearable devices at cold conditions.

1. Introduction

The development of flexible electronics and implantable medical devices has triggered an extensive demand for energy storage devices with high flexibility, reliable safety, and robust performance.¹⁻⁴ In the past several decades, effort has been devoted to wearable energy storage devices, yielding flexible capacitors and various solid-state rechargeable batteries.⁵⁻⁹ Among them, zinc ion batteries (ZIBs) with gel or solid-state electrolytes have attracted an tremendous attention since they can avoid conventional safety issues of rigid lithium-ion batteries, which may result flammable and poisonous leakage in accidents.¹⁰⁻¹³ In the most recent several years, numerous studies with various strategies to design solid state batteries (ssBs) have been published.¹⁴ For example, Tong *et al.* designed flexible ssBs using polyvinyl alcohol (PVA)/ZnCl₂/MnSO₄ gel electrolyte.¹⁵ The flexible ssBs retain a high discharge capacity under bending. However, PVA polymer-based hydrogel usually suffers from low ionic conductivity, resulting low-rate performance.¹⁶ Zhi *et al.* developed a novel polyacrylamide (PAM)-based hydrogel electrolyte with an ultrahigh ionic conductivity and robust mechanical properties.⁵ The ssBs offer excellent electrochemical as well as extreme safety performance after being cut and hammered. However, most reported ssBs cannot maintain high electrochemical performance and/or mechanical properties at very low temperatures. At present, most reported working temperatures for ssBs is regular room temperatures (about 25 °C).¹⁷ The main issue is that batteries sacrifice most of the capacity due to the freezing of electrolyte and sluggish ionic conductivity in cold conditions.¹⁸

In the past several years, various approaches have been applied to fabricate freeze-resistant energy storage devices.^{19, 20} One method is to increase the concentration of solute in electrolyte. The increased concentration can reduce the freezing point and improve the ionic conductivity at low temperatures. However, highly concentrated electrolyte can result in corrosion and undesirable reactions, leading to the capacity decaying and short cycling life.²¹ Another commonly used method is to add organic additives to widen the working temperature window

of the batteries. For example, Chen *et al.* introduced dimethyl sulfoxide (DMSO) as an additive in electrolyte of aqueous rechargeable alkali-ion batteries.¹⁸ Small amount of addition of DMSO in electrolyte can depress the freezing point of electrolyte and improve the low temperature performance of ZIBs.¹⁷ Another common used organic additive for freezing resistant is ethylene glycol (EG). For example, Zhi *et al.* introduced EG in hydrogel electrolyte of ZIBs. With the addition of EG, the Zn-MnO₂ ssBs show improved electrochemical performance and enhanced mechanical stability at the low temperature of -20 °C.¹⁷ However, due to high freezing point and high viscosity, EG cannot further facilitate the batteries to operate at much lower temperatures below -20 °C. ZIBs with the operation at temperatures lower than -60 °C have rarely been reported.

As a polar molecule, methanol has oxygen as the negative area, and hydrogen as the positive area. Due to similar polarity with water, methanol can be mixed with water in practically any ratios.²² In the binary solutions, methanol molecules form stable molecule clusters with H₂O molecules by strong hydrogen bonds, leading to a decreased saturation vapor pressure of water. Therefore, the freezing point of binary solutions is depressed significantly.²³ In 1964, Miler *et al.* studied the freezing point of a series of mixtures of different molar fractions of water/methanol mixtures.²⁴ Based on the published phase diagram, the eutectic molar concentration of methanol is about 80 *mol.* %. At the eutectic point, the freezing temperature of water/methanol mixture can reach as low as -116.2 °C. Since last century, methanol has been used as a traditional antifreeze agent in various industrial fields. For example, methanol has been applied as a well-known car radiator antifreeze for many years.^{25, 26} Moreover, due to the satisfactory chemical and physical properties, methanol has also been widely used as an antifreeze agent in car windshield washer fluid to prevent it from freezing in winters.²⁷ Considering the low freezing temperature and low cost, the idea of designing water/methanol hybrid electrolyte can offer a practically useful approach to improve the performance of zinc ion batteries in cold conditions.

ssZIBs based on hydrogel electrolyte are considered as a promising candidate for wearable energy storage devices due to the properties of high safety, high flexibility and robust performance.^{17, 10, 28, 29} However, due to the existence of water molecules in hydrogel electrolyte, it is inevitable for the hydrogel electrolytes to freeze and lose elasticity at the extremely cold environment.^{30, 31} As an abundant sustainable material, cellulose nanofibers (CNFs) have been widely utilized as traditional reinforcing agents in different composite materials.^{32, 33} The highly entangled network of CNFs can help stabilize the gels and improve hydrogel's ion transport. Moreover, incorporation of combined CNFs and hydrogel electrolyte into batteries can enhance compressibility, mechanical strength, and ionic conductivity.¹⁰ Polyacrylamide (PAM) has been used as the hydrogel polyelectrolyte matrix in supercapacitors due to its high ionic conductivity and high toughness.³⁴ In addition, owing to the presence of numerous hydroxyl groups, the methanol molecules and PAM chains can be anchored onto the surface of CNFs' skeleton, forming an integrated film with high flexibility and high ionic conductivity.

Herein, electrolyte with low freezing point is first designed using methanol and water hybrid solvent. And the freezing point of the hybrid solvent can be as low as $-100\text{ }^{\circ}\text{C}$. The Me56 hybrid electrolyte enables the high reversibility of the Zn anode due to the inhibition of Zn^{2+} solvation and the suppression of corrosion reactions during cycling.³⁵ With Me56 hybrid electrolyte, the MgVO/Zn batteries show excellent performance properties. At 10 A/g , the batteries can deliver the high specific capacity of 214 mAh/g for over 4000 cycles with the charging time of about only 1 minute at each cycle. Furthermore, CNF-PAM hydrogel membrane is also developed based on the Me56 electrolyte. The robust mechanical performance of the CNF-PAM hydrogel electrolyte can be maintained at low temperature, enabling the batteries to be workable under repeated bending, twisting in freezing conditions. At the extremely low temperature of $-60\text{ }^{\circ}\text{C}$, the ssBs still deliver a high specific capacity of 140 mAh/g at the current density of 10 mA/g , showing a much higher capacity than the batteries with aqueous electrolyte (0.8 mAh/g). This

developed CNF-PAM hydrogel electrolyte exhibiting a great potential to be applied in wearable devices at cold conditions.

2. Experiments

2.1 Preparation of cathode material for ZIBs

$\text{Mg}_{0.3}\text{V}_2\text{O}_5 \cdot 1.0\text{H}_2\text{O}$ nanofibers were prepared based on a hydrothermal method.^[36] First, 12 mLs of H_2O_2 (VWR, 30%) were diluted in 48 mL deionized water. Then, 1.091 grams of V_2O_5 (Acros Organics, 98%) were added into the H_2O_2 solution. After being stirred at 25 °C for 1 h, a red-colored solution was obtained. Next, 10 mLs of 4 mM $\text{Mg}(\text{CH}_3\text{COO})_2$ solution were dropwise added into the above solution with continuously stirring. Then, the solution was transferred to a Teflon-lined autoclave with heating at 200 °C for 48 h. After the autoclave was cooled, the red-colored precipitate was collected with centrifugation and washed with water and ethanol alcohol for three times, respectively. The products were finally obtained after being dried at 70 °C for overnight.

2.2 Preparation of methanol and water hybrid electrolyte for ZIBs

Two mL of methanol and water mixed solvent were prepared with 56% and 80% molar ratio of methanol, respectively. Then, 0.727 grams of $\text{Zn}(\text{CF}_3\text{SO}_3)_2$ (>98%, TCI America) were added into the mixed solvent.³⁷ After $\text{Zn}(\text{CF}_3\text{SO}_3)_2$ was dissolved, the mixed solvent electrolyte was obtained. The hybrid electrolytes with methanol molar ratio of 0%, 36%, 56%, 80% and 100% are designated as Me0, Me36, Me56, Me80 and Me100, respectively.

2.3 Preparation of CNF-PAM hydrogel electrolyte for solid-state zinc ion batteries

CNF-PAM hydrogel electrolyte was prepared according to a previously published method.³⁸ First, 0.02 mol acrylamide (AM) monomers, 0.06 mol Ammonium persulfate and 0.8 mg N, N'-methylenebisacrylamide were dissolved in 4 mL deionized water. Then, 0.266 grams of CNFs (15 wt % in water suspension, University of Maine, Orono, ME, USA) were added into the prepared chemical solution. After being stirred for half an hour at 25 °C, the mixture was cast onto a glass mold. After being heated at 60 °C for half an hour, the hydrogel membrane

was obtained. Finally, the CNF-PAM hydrogel electrolyte was obtained with the membrane being soaked in the Me56 hybrid electrolyte for one hour. The solvent content of the final obtained CNF-PAM hydrogel electrolyte was about 60 wt%.

3. Characterization

The sessile drop contact angle technique (goniometry, FTA1000, First Ten Angstroms, Portsmouth, VA, USA) was applied to study the wettability of the formulated hybrid electrolytes. The Energy dispersive spectroscopic (EDS) mappings, morphology change of the Zn anode and microstructure of the synthesized MgVO cathode were investigated by using a FEI Quanta 3D FEG field emission scanning electron microscope (SEM) (FEI, Boston, MA, USA). The crystallographic structure and selected area diffraction patterns (SAED) were observed by a JEM-1400 (JEOL, Peabody, MA). The XRD measurement was carried out on a Rigaku MiniFlex XRD instrument (RIGAKU, Austin, TX, USA). Thermogravimetric analysis (TGA) was conducted by Q50 (TA Instruments, New Castle, DE, USA). X-ray photoelectron spectroscopy (XPS) analysis was collected in an AXIS165 spectrometer (MRFN, Manchester, UK). Fourier Transform Infrared (FTIR) spectroscopy was conducted by using a Thermo Scientific Nicolet 6700 (Waltham, Boston, MA, USA).

Zn/Zn symmetrical batteries were assembled using two identical zinc metal foils separated with glass fiber membrane. Zn plating and stripping processes were studied with galvanostatic charge and discharge at the current density ranging from 1 mA/cm² to 5 mA/cm². Full cells were assembled using the prepared Mg_{0.3}V₂O₅·1.0H₂O nanofibers as cathode, zinc metal as the anode, prepared Me56 as electrolyte, glassfiber membrane as separator. Electrochemical tests were conducted on an eight-channel LAND battery analyzer (CT3001A, LAND Electronics Corporation, Wuhan, China). Cyclic voltammetry (CV) measurements and Electrochemical impedance spectroscopy (EIS) data were performed on an electrochemical workstation (CHI 760e). The solid-

state batteries were assembled using the PAM-CNF film as the electrolyte and separator. Freeze-resistant test was carried out to cycle the batteries at $-20\text{ }^{\circ}\text{C}$ or $-60\text{ }^{\circ}\text{C}$ in a ultra-low temperature freezer (Whirlpool, Benton Harbor, MI, USA). The test was done by setting the freezer to the target temperature first ($-20\text{ }^{\circ}\text{C}$ or $-60\text{ }^{\circ}\text{C}$). The batteries were then placed in the freezer for half an hour to ensure the uniform temperature reached inside the batteries. Then, the batteries were connected to the LAND battery analyzer for the cycling test.

4. Results and Discussion

The freezing points of methanol and water are -97.6 and $0\text{ }^{\circ}\text{C}$, respectively. The mixture of methanol and water can thus achieve a lower freezing point. Figure S1 shows the DSC results of the electrolyte solvent SMe56 (SMex, without $\text{Zn}(\text{CF}_3\text{SO}_3)_2$, methanol content 56 mol.%) and SMe80 (without $\text{Zn}(\text{CF}_3\text{SO}_3)_2$, methanol content 80 mol.%). As shown in the phase diagram (Figure 1a), with the methanol fraction of 36%, the freezing point of SMe36 is about $-50\text{ }^{\circ}\text{C}$. With the molar ratio of methanol increased to 56 % and 80 %, SMe56 and SMe80 achieve eutectic freezing points of $-98.6\text{ }^{\circ}\text{C}$ and $-114\text{ }^{\circ}\text{C}$, respectively. The DSC results of SMe56 and SMe80 match well with the phase diagram published previously.^[24] As shown in the FTIR spectrum (Figure 1b), three electrolytes (i.e., Me0, Me56, and Me100) show a broad and strong peak at $3200\text{-}3500\text{ cm}^{-1}$, which is assigned to the OH stretching vibration. Compared with Me0 and Me56, the OH stretching vibration of pure methanol electrolyte shows a slight red shift. In Figure 1b, the other two sharp peaks shown at 2843 and 2953 cm^{-1} are attributed to the CH_3 stretching modes of Me56 and Me100 electrolytes. Figure 1c shows the characteristic peak for bending vibration of H_2O at $1600\text{-}1700\text{ cm}^{-1}$. Compared with that for Me0, a slight blue shift is observed in the Me56 and Me100 electrolytes. From the Raman results shown in Figure 1d and 1g, a slight red shift of CH stretching ($2800\text{-}3000\text{ cm}^{-1}$) and a slight blue shift of C-OH bending ($1450\text{-}1480\text{ cm}^{-1}$) are revealed, respectively. The phenomenon in the FTIR and

Raman results can be explained by the interaction between COH in methanol and OH in water. The higher electron density of COH in methanol and lower electron density of OH in water reveal the hydrogen bonding interaction between oxygen atoms in methanol and hydrogen atoms in water. Figures 1e and 1h show the ^1H NMR spectra of mixed electrolytes, and Figures 1f and 1i show the ^1H NMR spectra of the hybrid solvent. The ^1H peak of pure water is located at 4.789 ppm, and it slightly shifts to lower field with a larger σ value (4.800 ppm) after dissolving of 2M $\text{Zn}(\text{CF}_3\text{SO}_3)_2$. The ^1H resonance from OH and CH_3 of pure methanol is at 4.949 and 3.413 ppm, respectively. After dissolving 2 M $\text{Zn}(\text{CF}_3\text{SO}_3)_2$, the two peaks move to 4.871 ppm and 2.925 ppm, respectively. These results indicate that the electron density of ^1H from water decreases with the dissolving of 2M $\text{Zn}(\text{CF}_3\text{SO}_3)_2$. The electron density of ^1H from methanol increases after the dissolving of 2M $\text{Zn}(\text{CF}_3\text{SO}_3)_2$. This proves that the solvation interaction of Zn^{2+} with the O atoms in H_2O molecules is much stronger than that in methanol molecules. As shown in Figure 1e, with increase of the methanol content in the hybrid electrolyte, the ^1H resonance shifts to a lower field. In Me56, the ^1H resonance reaches 4.87 ppm with chemical shift ($\Delta\sigma = 0.07$ ppm) from the Me0 system ($\sigma_1 = 4.8$ ppm). In contrast, as the methanol content increases in mixed solvent SMe, the chemical shift ($\Delta\sigma = 0.009$ ppm) is much smaller. This indicates that the solvation interaction with zinc ions can enhance the hydrogen bonding between methanol and water, leading to larger chemical shift of ^1H from water.

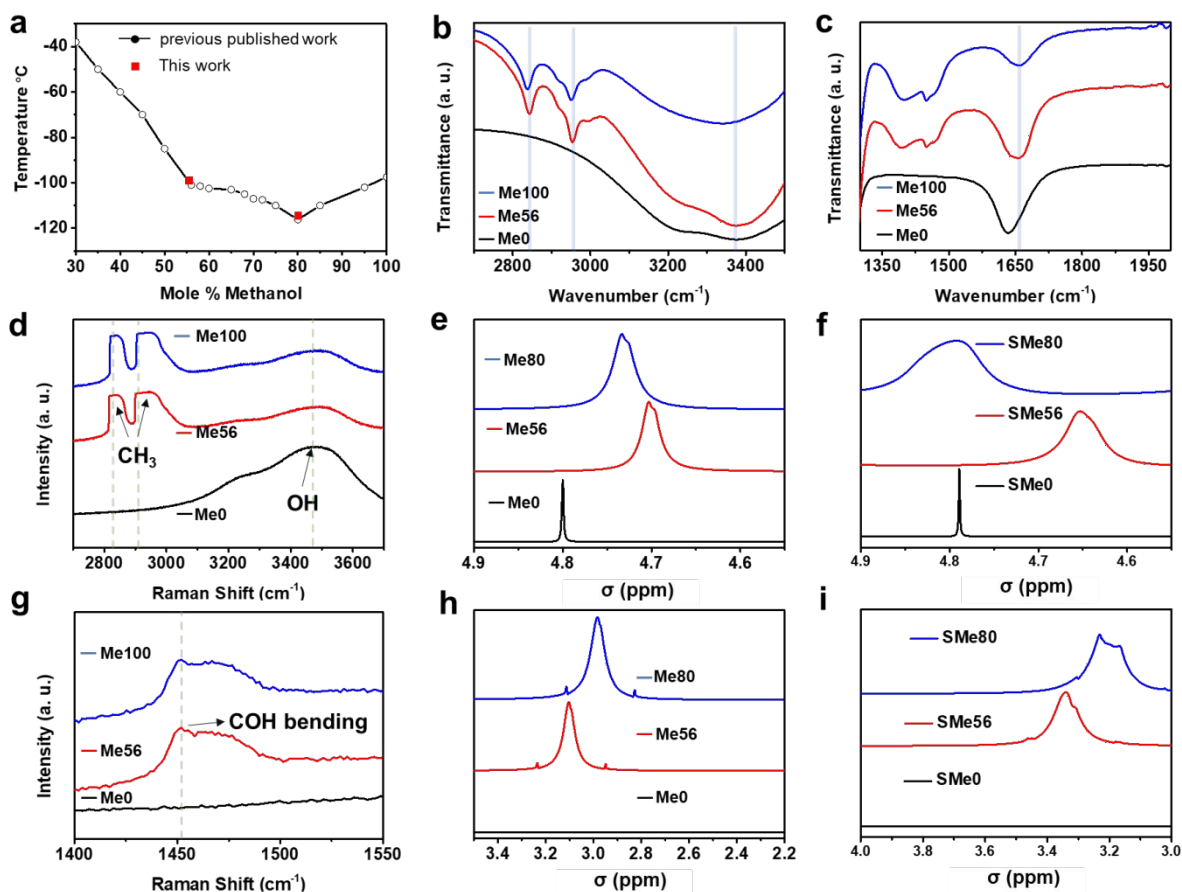


Figure 1. (a) The solid-liquid phase diagram of methanol-water. Solid circles are data from previously published work.^[24] (b, d) FTIR spectrum and (c, g) Raman spectra of pure methanol, methanol/water mixture and pure aqueous electrolyte. (e, h) ¹H NMR spectrum from H₂O for mixed electrolyte. (f, i) ¹H NMR spectrum from H₂O for hybrid solvent (SMex, without Zn(CF₃SO₃)₂).

Electrochemical stability and reversibility of zinc anode in hybrid electrolytes

The wettability on zinc foil has a significant effect on the energy barrier for zinc nucleation during the plating and stripping processes.³⁹ As displayed in Figure 2a, zinc metal shows a high contact angle of 73.50° with aqueous electrolyte. The contact angle significantly decreases with hybrid electrolytes. For Me36 and Me56 hybrid electrolytes, zinc metal shows decreased contact angles of 46.89° and 19.10°, respectively. For a pure methanol electrolyte, zinc metal has a low angle of 15.67°. The reduced contact angles confirm that methanol molecules are more likely to be absorbed on the surface of zinc metals to further affect the hydrogen evolution

and Zn nucleation.^{40, 41} Linear sweep voltammetry (LSV) response curves were collected in different electrolytes to study the impact of methanol on the H₂ evolution in hybrid electrolytes. As shown in Figure 2e, the aqueous electrolyte exhibits an onset potential of -1.0 V for H₂ evolution. For the Me 36 hybrid electrolyte, the onset potential increases to -1.14 V and the current is also much lower. For the Me56 and pure methanol electrolyte, no obvious H₂ evolution could be observed. Furthermore, Zn//Ti half cells were also tested. The LSV curves in Figure 2f demonstrate the significantly increased corrosion potential and oxygen evolution reaction potential in the Me56 hybrid electrolyte, confirming the positive impact of the addition of methanol. The free water and coordinated water in Zn²⁺ solvation interact with methanol molecules, leading to lower water activity and weakened Zn²⁺ solvation. Therefore, the H₂ evolution is inhibited, and the corrosion reaction is suppressed.

Figure 2g illustrates the voltage profile of the Zn//Zn symmetric cells at the current densities ranging from 1 to 5 mA/cm². Compared with the batteries using aqueous electrolyte, the batteries based on the Me56 hybrid electrolyte exhibit a flat and stable voltage plateau at various currents. With the current density increased from 2 to 3 mA/cm², there is an abrupt voltage drop in the batteries with the Me0 aqueous electrolyte. This is attributed to the short-circuit of batteries due to the formation of Zn dendrites during the Zn stripping and plating processes. The long-term Zn stripping and plating study data and related voltage profile are displayed in Figure 2i and j. During the long-term Zn stripping and plating cycles, the voltage profile of the batteries with Me56 electrolyte does not exhibit any voltage hysteresis after 500 hours. In contrast, the batteries with the Me0 aqueous electrolyte exhibits a large fluctuation on voltage and obvious short circuit after about 30 cycles, probably due to the aggravated dendritic Zn growth during the cycling. In the Me56 antisolvent electrolyte, the inhibition of Zn dendrite growth significantly extends the cycling performance of batteries. The related voltage profile is shown in Figure 2j. The deposition potential for Me56 is a little bit higher than that of Me0. This is attributed to the sluggish desolvation process with the addition of methanol in electrolyte.

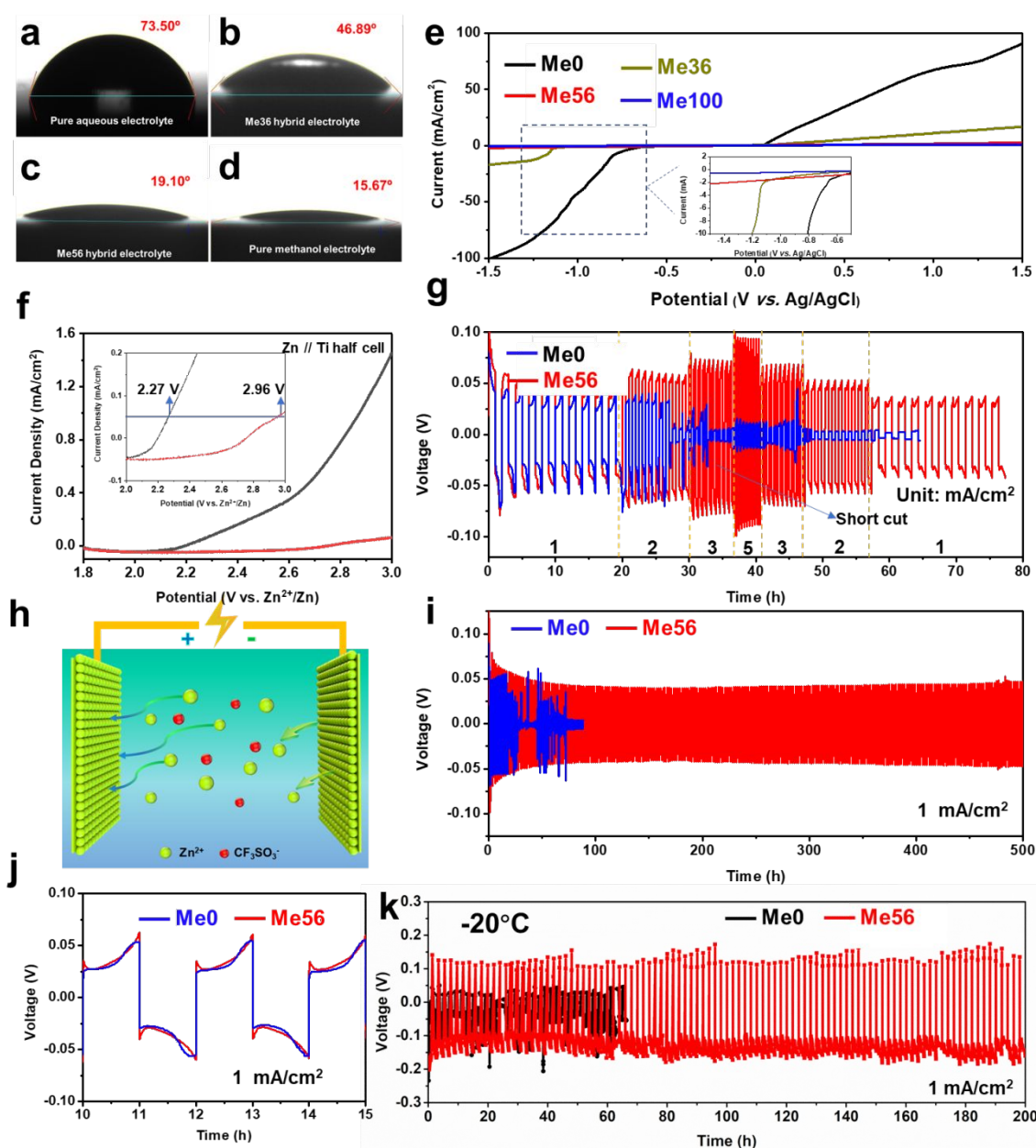


Figure 2. Contact angle data on zinc anode (a) pure aqueous electrolyte, (b) Me36, (c) Me56 hybrid electrolyte, and (d) pure methanol electrolyte. (e) The LSV curves for different electrolyte at 100 mV/s. (f) The LSV curves of Zn//Ti half cells tested in aqueous and Me56 hybrid electrolyte at the scan rate of 1 mV/s. (g) Voltage profiles for Zn//Zn symmetric batteries at the current density from 1 to 5 mA/cm² in different electrolytes. (h) Schematic of Zn//Zn symmetric cells. (i) Cycling stability and (j) voltage profiles for Zn//Zn symmetric batteries at 1 mA/cm² at 25°C. (k) Cycling stability of Zn//Zn symmetric cells at -20 °C.

As shown in the voltage profile (Figure S2), the Zn//Zn symmetric cell batteries with Me56 electrolyte exhibit smooth voltage-capacity curves and stable Zn plating / stripping processes evaluated at -20 °C. In contrast, the batteries with Me0 electrolyte show a large fluctuation. This is attributed to the partial freezing of aqueous electrolyte at low temperatures. In addition, the symmetric batteries with Me56 electrolyte show a highly reversible plating and stripping process during long cycles. The batteries with the Me56 hybrid electrolyte exhibit a steady polarization potential (about 0.15 V) for over 200 hours at -20 °C. In contrast, cells with Me0 aqueous electrolyte shows an apparent short-cut after 60 cycles. As displayed in Figure S3a and b, with Me0 aqueous electrolyte, the surface of Zn electrodes was seriously damaged after 50 cycles. The deposited Zn is dendritic and porous, leading to the polarization and limited Zn reversibility. In contrast, with Me56 antisolvent electrolyte, the zinc deposition is smooth and homogeneous without the formation of Zn dendrites (Figure S3c and d). This is probably attributed to the modified deposition orientation of zinc. As shown in the wettability data (Figure 2a), methanol molecules are more likely to be absorbed on the surface of zinc metals, which significantly affects the Zn deposition orientation during plating. Based on the DFT calculation from previous publications, methanol molecules are more likely to induce the Zn deposition on the (002) facet, leading to a smooth and homogeneous Zn deposition without Zn dendrites. These results confirm that the Me56 hybrid electrolyte can change the deposition of Zn, significantly avoid the Zn corrosion, and hinder the H₂ evolution.

Performance of zinc ion batteries with hybrid electrolytes

As shown in Figure S5a, all the CV curves of MgVO/Zn batteries with different hybrid electrolytes display two pairs of redox peaks at around 0.92/1.25 V, 0.50/0.80 V. The cathodic peaks at 0.92 and 0.50 V are attributed to the insertion of Zn ions into the interlayer space of MgVO lattice and the related reduction of vanadium. The two anodic peaks at 1.25 and 0.8 V are ascribed to the oxidation of vanadium and returning into MgVO phase with the extraction of zinc ions. For different hybrid electrolytes, the peak position and the shape of CV curves are

very close, revealing the same electrochemical reactions with different composition of hybrid electrolytes. The galvanostatic charge-discharge plots at 200 mA/g are shown in Figure 3a. With hybrid electrolytes of Me0, Me36, ME56 and Me100, the batteries can deliver the specific capacity of 350.8, 341.7, 336.1, and 324.9 mAh/g, respectively. The closed capacity value and consistent plateaus in CV curves reveal the similar battery performance with different hybrid electrolytes at 25 °C. With Me56 hybrid electrolyte, the batteries deliver the high specific capacity of 214 mAh/g after 4000 cycles at 10 A/g (charging time: about 1 minute) and almost 100% Coulombic efficiency, account 115% of the initial specific capacity, showing extraordinary cycling durability at high current density. The excellent high current performance attributes to the large interlayer space of MgVO crystal structure, which can accommodate the fast intercalation of zinc ions.

Figure 3c displays the charge/discharge profiles with Me56 electrolyte for various temperatures at 0.5 A/g. At 25 °C, the batteries with the Me56 electrolyte deliver a specific capacity of 321.4 mAh/g. At 3 and -20 °C, the capacity slightly decays to 290.0 and 211.6 mAh/g, respectively, showing favorable low-temperature capacities. Figure 3d shows the rate performance of batteries with different hybrid electrolytes at -20 °C. At the current densities of 0.2, 0.5, 1, 2 and 5 A/g, batteries with Me56 electrolyte deliver the specific capacity of 284.9, 251.2, 219.6, 166.2, and 59.5 mAh/g, respectively, showing much higher capacity than that with Me80 and Me100 at each current density. Figure 3e shows the cycling performance at current density of 1A/g at -20 °C. After 120 cycles, the MgVO/Zn batteries with Me56 electrolyte deliver the high specific capacity of 201.4 mAh/g, showing favorable cycling stability in cold condition. To further explore the electrochemical performance at super-low temperature, the batteries were tested at temperature of -60 °C. Figure 3f displays the charge-discharge profiles of batteries with different hybrid electrolytes at current density of 10 mA/g at -60 °C. Compared with Me0 (1.59 mAh/g), Me80 (79.8 mAh/g) and Me100 (20.1 mAh/g), ZIBs with Me56 electrolyte deliver the highest specific capacity of 141.53 mAh/g. The batteries

with pure aqueous electrolyte sacrifice most of the capacity due to the freezing of electrolyte at super low temperature. Hybrid electrolytes with low freezing point make batteries still workable at this super cold condition. Figure 3g shows the rate performance of batteries with different hybrid electrolytes at $-60\text{ }^{\circ}\text{C}$. Compared with low specific capacity in Me80 and Me 100 electrolytes, the batteries with Me56 electrolyte deliver much higher specific capacity of 137.5, 100.8, 62.8, and 48.5 mAh/g at each current density of 10, 20, 50 and 100 mA/g respectively, showing remarkable low-temperature capacity. Figure 3h shows the cycling performance of ZIBs with different hybrid electrolytes at the current density of 10 mA/g. The MgVO/Zn batteries with electrolytes of Me0, Me56, Me80, and Me100 deliver the initial specific capacity of 0.04, 140.0, 70.7, and 24 mAh/g, respectively. After 100 cycles, batteries with Me56 electrolytes can still maintain the specific capacity of 128 mAh/g, which is much higher than that in electrolytes of Me0 (0.0028 mAh/g), Me80 (79.0 mAh/g), or Me100 (10.4 mAh/g), displaying an excellent capacity retention rate. Remarkably, an outstanding energy density with high power density is also obtained for the MgVO/Zn batteries with the Me56 electrolyte. As shown in the Ragone plot - Figure 3i, at $-20\text{ }^{\circ}\text{C}$, the ZIBs deliver an outstanding energy density of 28.8 Wh/Kg with a high-power density of 2341.5 W/Kg, which is superior to those previously published work on batteries at subzero temperature.⁴²⁻⁴⁵ Moreover, at the low temperature of $-60\text{ }^{\circ}\text{C}$, the MgVO/Zn with the Me56 electrolyte can still deliver an excellent energy density of 16.7 Wh/Kg with a high-power density of 47.9 W/Kg. As shown in Figure 3j, batteries with Me56 electrolytes deliver the initial specific capacity of 66 mAh/g. After 800 cycles, it can still maintain the capacity of 63 mAh/g, with capacity retention of 95.45%, showing high capacity with long cycling life. Compared with the battery performance with Me80 and Me100 electrolytes, ZIBs with Me56 electrolyte show much higher capacity and longer cycling life in cold conditions. This is attributed to the higher water content in Me56 electrolyte. The co-insertion of water molecules can facilitate the insertion of bivalent zinc ions at the interface and the host material as well. As reported by Stoddart *et al.*, the co-intercalation

of water molecules can reduce the Coulombic repulsion at the interface of electrode and electrolyte due to the charge-screen effect, leading to higher capacity retention and longer cycling life.⁴⁶

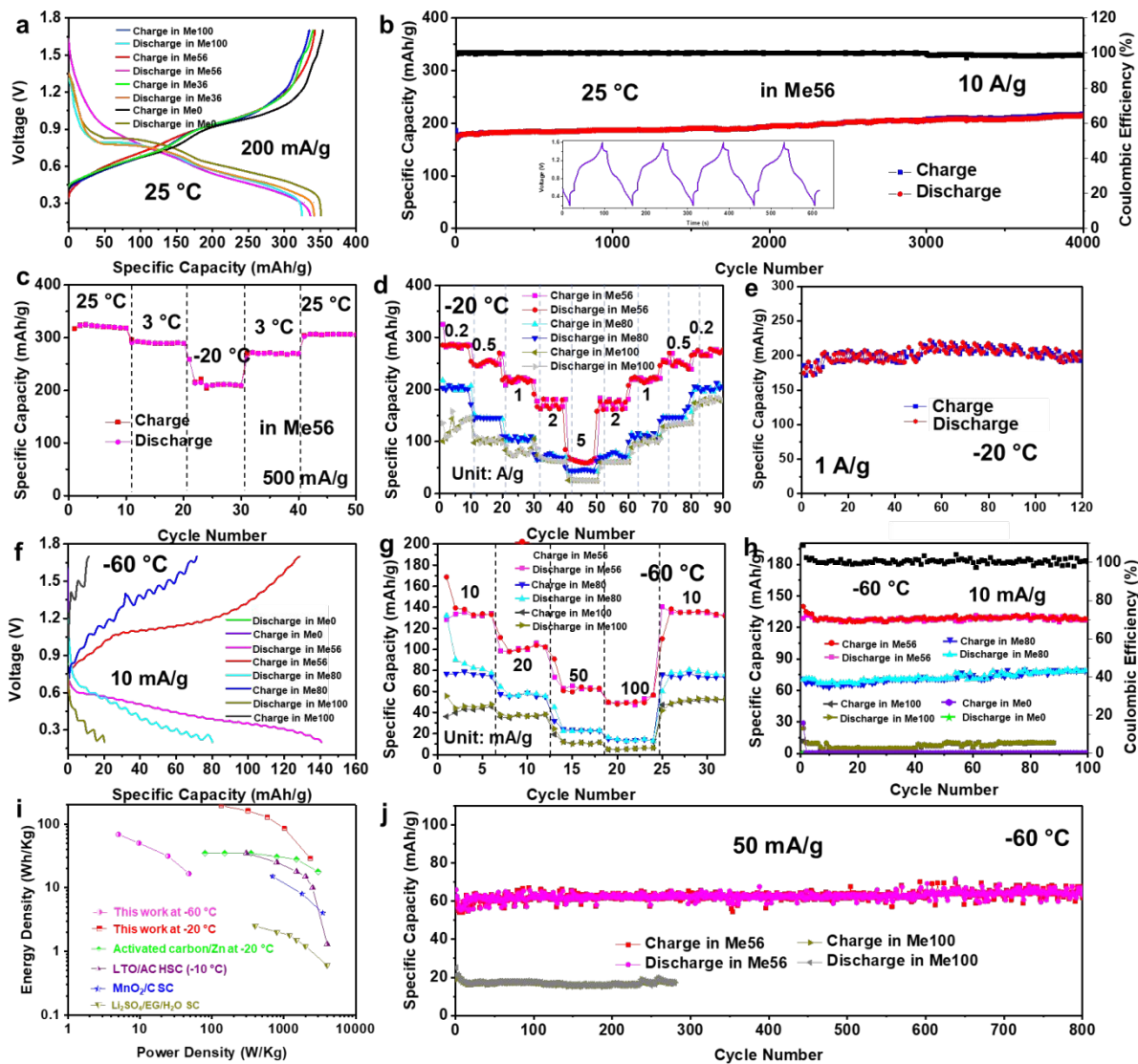


Figure 3. Electrochemical performance data of MgVO/Zn batteries with different hybrid electrolytes (a) Charge-discharge profiles at 200 mA/g and (b) long cycling performance with Me56 electrolyte (-at 10 A/g. (c) Specific capacities at different temperature with current density of 500 mA/g. (d) Rate performance at -20 °C. (e) cycling performance at 1A/g at -20 °C. (f) Charge-discharge profiles with current density of 10 mA/g at -60 °C. (g) Rate performance at -60 °C. (h) Cycling stability with current density of 10 mA/g. (i) Ragone plot of MgVO/Zn

batteries in comparison with other batteries and supercapacitors. (j) Cycling performance at current density of 50 mA/g at -60 °C.

Kinetics Analysis

As shown in the CV curves (Figure S6a), with the scan rate increased from 0.1 to 5.0 mV/s, the anodic peaks move to higher potential and the cathodic peaks move to lower potential, which is due to the increase of diffusion resistance at high scan rate. Electrochemical kinetics can be analyzed *via* power-law formula as:

$$i = av^b \quad (1)$$

where, a and b are parameters, v is the scan rate (V/s), and i is the current (A). The value of b represents the charge storage reaction. If b value is closed to 0.5, the electrochemical reaction is mainly controlled by the diffusion-limited process. If b value reaches 1, it is dominated by surface capacitive process. Figure S6b shows the plots of $\log(i)$ versus $\log(v)$. The b value calculated from the slope of peak 1 and 2 are 0.713 and 0.662, respectively, suggesting that both diffusion and capacitive processes contribute the capacity. GITT was further measured for the batteries with different electrolytes and the results are shown in Figure S7-8. The diffusion coefficient $D_{\text{Zn}^{2+}}$ (cm^2/s) was calculated based on the equation below:

$$D_{\text{Zn}^{2+}} = \frac{4l^2}{\pi t} \left(\frac{\Delta E_s}{\Delta E_t} \right)^2 \quad (2)$$

where, t is the time of current pulse, l is the thickness of cathode, ΔE_s is the variation of steady-state potential at each step, and ΔE_t is the potential change of a one-step GITT test after eliminating the iR drop. As shown in Figure S7-8, the average value of $D_{\text{Zn}^{2+}}$ for discharging and charging process is about $1 \times 10^{-7.05}$ and $1 \times 10^{-7.17}$ cm^2/s respectively. The values are much higher than these for ZIBs with pure methanol electrolyte ($1 \times 10^{-7.29}$ for discharging and $1 \times 10^{-7.20}$ cm^2/s for charging) and comparable with ZIBs with pure aqueous electrolyte ($1 \times 10^{-7.04}$ for discharging and $1 \times 10^{-7.14}$ cm^2/s for charging). The high diffusion coefficients in aqueous and hybrid electrolytes are attributed to the water molecules in electrolyte. It is believed that the

intercalation mechanism involves the co-intercalation of zinc ions with water molecules into the lattice of the host.⁴⁷ As reported in previously published literature, the hydrated intercalation can significantly mitigate the desolvation energy penalty at the interface between electrolyte and electrode. For the batteries with organic electrolyte, such as pure methanol, carrier ions at interface are desolvated with high overpotential. This overpotential is even higher for multivalent cations (Zn^{2+}) owing to the high electrostatic interaction between the multivalent cations and solvent molecules. These cations with high charge densities can hinder the diffusion of charge carriers *via* high electrostatic interaction with the host lattice. However, these effects can be significantly alleviated with the assistance of water molecules cointercalated, which can shield the electrostatic interactions between host material and charge carriers. Hydrated interaction avoids this energy loss, leading to facile diffusion of zinc ions at the interface of host lattice. EIS results further confirm the lower resistance in batteries with water contained. As shown in the EIS spectra (Figure S9), the batteries with Me100 electrolyte show a high charge transfer resistance of 511 Ω . With the increased ratio of water, the resistances of Me 56 and Me0 are significantly reduced to 135 and 210 Ω , respectively, due to the effect of hydrated interaction.

Performance of Solid-state Zinc Ion Batteries Based on CNF-PAM Hydrogel electrolyte

Figure 4a shows a schematic illustration of the designed MgVO/Zn ssBs. Figure 4b shows the CV curves of MgVO/Zn ssBs in the first cycle. Two reduction peaks are located at 0.73 and 0.3 V and two corresponding anodic peaks are resolved at 0.78 and 1.18 V, which is very closed to the peak positions in MgVO/Zn batteries with liquid electrolyte, suggesting similar redox reactions. Figures 4c and 4f show the cycling performance at the current density of 500 mA/g and 1 A/g at 25°C, respectively. At 500 mA/g, MgVO/Zn ssBs can deliver the high specific capacity of 336 mAh/g after 50 cycles, which is closed to the capacity of the aqueous batteries. At 1 A/g, the MgVO/Zn ssBs can provide the initial specific capacity of 265 mAh/g. After 500 cycles, the specific capacity can still be maintained at 268 mAh/g, showing excellent long

cycling stability. Moreover, the synthesized CNF-PAM hydrogel electrolyte also shows excellent mechanical properties. Figure S10 shows the tensile stress-strain curve of the CNF-PAM hydrogel. The hydrogel can reach 247.6 kPa with the strain of 687%. After storage at -20 °C for two days, mechanical properties are still maintained well (Figure 4d). High elasticity sustains the deformation of elongation, bending and twisting. Moreover, the excellent mechanical properties of CNF-PAM hydrogel membrane enable the high flexibility of the designed solid-state batteries.²⁹ As shown in the optical photos (Figure 4e) and the videos s in Supporting Information II and III, the red LED array light up by MgVO/Zn ssBs under bending or twisting. The solid-state batteries are still workable under repeated bending and twisting, demonstrating high flexibility and stability of the designed ssZIBs. The electrochemical performance of ssZIBs under low temperature was further investigated. From the cycling performance shown in Figure 4g, the MgVO/Zn ssBs delivered the initial discharge capacity of 178 mA/g at 1 A/g at -20 °C. After 50 cycles, the batteries still maintained the capacity of 145 mAh/g, with 81.5 % of the initial capacity retained. Figures 4i and j show the charge-discharge profiles and cycling performance at -60 °C. As shown in Figure 4i, at the current density of 10 mA/g, MgVO/Zn ssBs can still deliver the specific capacity of more than 130 mAh/g, exhibiting high capacity under low temperature. At 30 mA/g, the ssBs can provide the initial capacity at 74 mAh/g. After 60 cycles, the specific capacity can be still maintained at 58.8 mAh/g, retaining 79.3% of the initial capacity.

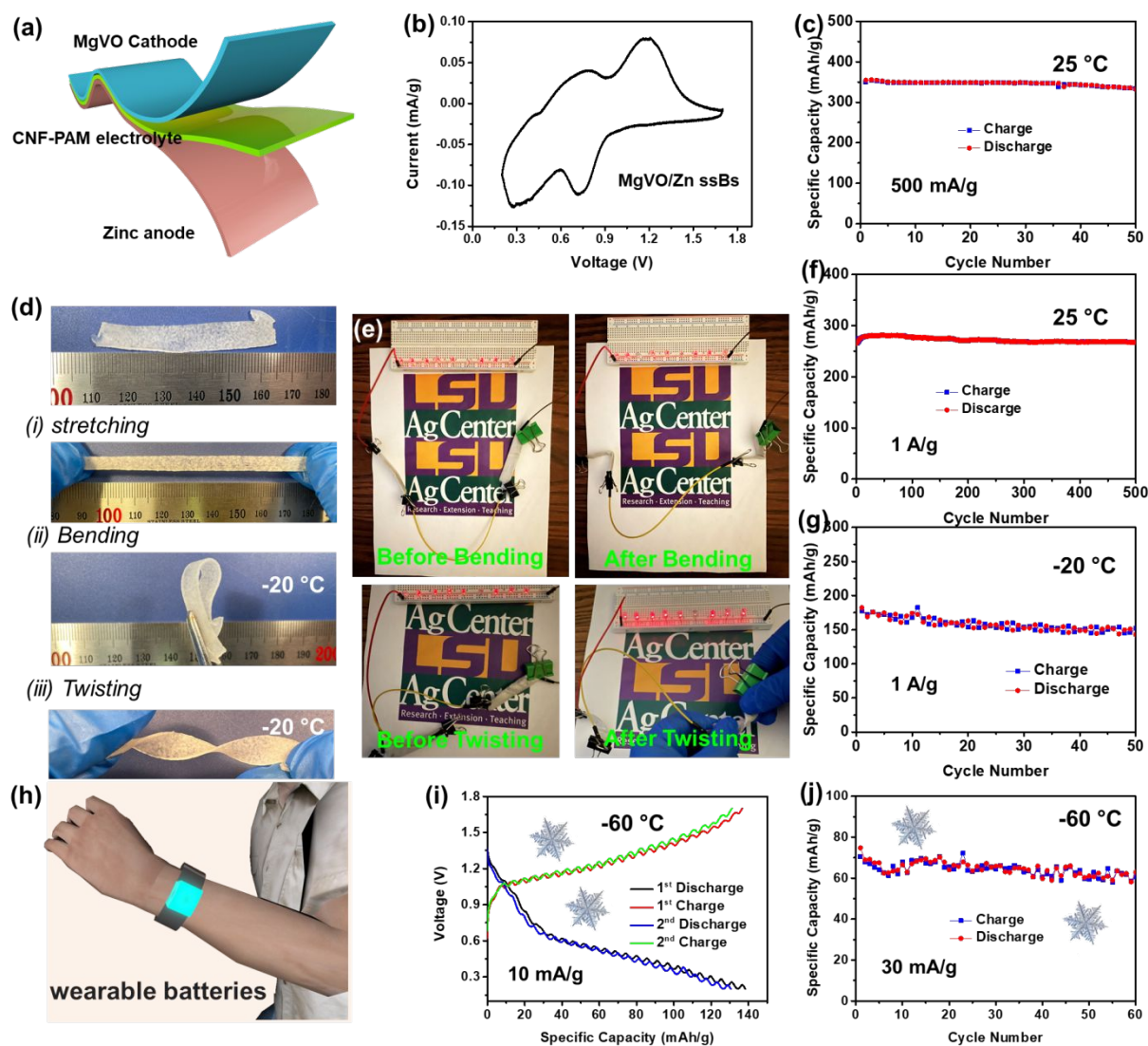


Figure 4. Electrochemical performance of MgVO/Zn ssBs based on CNF-PAM hydrogel electrolyte. (a) schematic illustration of the designed MgVO/Zn ssBs, (b) CV curves collected at 0.1mV/s, cycling performance at (c) 500 mA/g, (f) 1 A/g under room temperature (25 °C), (d) the optical photos of the prepared CNF-PAM hydrogel membrane under (i) stretching, (ii) bending and (iii) twisting after freezing at -20 °C for two days, (e) optical photos of the red LED array light up by bending or twisting MgVO/Zn ssBs. Cycling performance at the current density of (g) 500 mA/g at -20 °C, (i) charge-discharge profiles at 10 mA/g at -60 °C, (j) cycling performance at 30 mA/g at -60 °C. (h) schematic illustration of wearable batteries under cold conditions.

Electrochemical Mechanism

As shown in the Galvanostatic voltage-capacity profiles (Figure 5a), the MgVO cathode was tested in hybrid electrolytes with different compositions: Me100 (100 mol % methanol), Me 56 (56 mol % methanol in water), Me 36 (36 mol % methanol in water) and Me0 (100 mol % water) with 1M $\text{Zn}(\text{CF}_3\text{SO}_3)_2$. At 1 A/g, the MgVO/Zn batteries with Me100 electrolyte can deliver the specific capacity of 207 mAh/g. Obviously, an increase in capacity can be observed with the increase of water content in electrolyte. The capacity of MgVO/Zn batteries with pure aqueous electrolyte can reach as high as 303.7 mAh/g. From this trend, we can learn that the amount of water has a significant effect on the performance of Zn batteries. To confirm the cointercalation of water into the cathode material, ex-situ FTIR spectra of MgVO sample at initial, discharged and charged states were investigated and the data is shown in Figure 5b. Compared with that at initial and charged states, the MgVO sample at discharged state shows an increased presence of water at the wavenumber of 3500 cm^{-1} . This phenomenon of hydrated intercalation was also observed in the previously published reports.⁴⁸⁻⁵⁰ XPS, XRD, Raman spectrum and HRTEM were applied to investigate the electrochemical mechanism. As shown in Figure 5c, high-resolution XPS spectra of V 2p were obtained at the initial, fully discharge and charge states. Upon discharging state, the V^{5+} signal at 516.8 eV decreases significantly. Meanwhile, the V^{4+} signal at 516.3 eV strongly increases. This is due to the reduction of V with the insertion of zinc ions into the MgVO lattice. At the fully charged state, V^{5+} signal returns to the major species, revealing reversible electrochemical redox reaction. Figure S11 shows the Zn 2p core level spectra at the initial, fully discharge and charge states. The intensity of Zn 2p at discharge state is much higher than that at initial and charge states, suggesting the insertion/extraction of Zn^{2+} ions during charging and discharging. The Mg 2s region at different states is displayed in Figure S12. As shown in Figure S12, compared with initial state, the intensity of Mg 2s signal at 1st charge state is apparently lower, suggesting that Mg^{2+} ions were deintercalated during the initial cycle. To further confirm the deintercalation of Mg^{2+} ions

during cycles, we tested the Mg 2s signal on zinc anode side after 800 cycles. As shown in Figure S12c, the strong Mg 2s core level demonstrates the deintercalation of Mg^{2+} ions from MgVO cathode and deposition on the zinc anode. This phenomenon is also observed in $\text{Ag}_{0.4}\text{V}_2\text{O}_5$ and $\text{Na}_3\text{V}_2(\text{PO}_4)_3$ for ZIBs, (i.e., the displacement/intercalation reaction mechanism).^{51, 52} Figure 5e and f show the XRD patterns of MgVO cathode at different charge/discharge states during the initial cycle at 0.2 A/g. The peak at 18° attributes to PTFE binder utilized for electrode preparation. As displayed in Figure 5a, the intensity of main peak (001) at 7.31° decreased dramatically during the initial discharge process. This is due to the decrease of crystallinity and structural change with the insertion of zinc ions. Moreover, at the fully discharge state, the obvious new peaks appeared 26.0° and 33.5° can be designated to the reflection from the (001) to (005) planes of $\text{Zn}_x\text{V}_2\text{O}_5 \cdot n\text{H}_2\text{O}$,^{53, 54} suggesting the formation of new phase transformed from the monoclinic MgVO. In addition, as shown in the magnified XRD patterns (Figure 5f), the (001) peak at 7.31° moves to higher angles while discharging. This is probably attributed to the contraction of the interlayer spacing at the discharge state. With the zinc ions and water molecules coming into the lattice, the formation of hydrogen bonds between the structural oxygen and zinc ions pulls the layers closer. At the fully charged state, the two new peaks disappear, and the main (001) peak moves back to 7.31° , suggesting high reversibility of the structural change during the discharging and charging process. Moreover, as reported by Choi *et al.*, water molecules are the key factor to determine the coordination sites for zinc.⁵⁵ With water molecules, octahedral coordination is preferred, causing minimal distortion on the host framework. Raman spectra was also applied to investigate the structure change and the results are shown in Figure 5g. At the fully discharge state, the main peak at 138.9 cm^{-1} decreases while the new peak appeared at 861.0 cm^{-1} strengthens remarkably. This is attributed to the significant increase of the long-range disorder of the vanadium oxygen layers along the plane with the insertion of Zn^{2+} ions. Moreover, the peaks at $281.3, 405.9, 519.5\text{ cm}^{-1}$ shifts to lower frequency at $250.9, 368.9$ and 495.6 cm^{-1} , respectively. The blue shifts of these three peaks are due to the lengthening of the V-O₁ and V-

O_2 bonds for the new $Zn_xV_2O_5 \cdot nH_2O$ phase. The inserted water molecules and zinc ions are bonded with lattice oxygen, leading to the formation of more H-bonding. The H-bonding leads to decrease the strength of V=O and strengthen the V-O-V, resulting the shift of the bond vibration. To further confirm the phase transformation during discharge and charge, the HRTEM images at different states were taken. As displayed in Figure 5h, the lattice fringe of 0.204 nm can be indexed to the (006) plane of the original MgVO phase. At the discharge state, the appeared broaden lattice fringe of 0.374 nm is apparently attributed to the new phase with the intercalation of zinc ions. At the fully charged state, the lattice fringe returns to about 0.209 nm, indicating high reversibility of the structure change with the insertion/extraction of zinc ions.

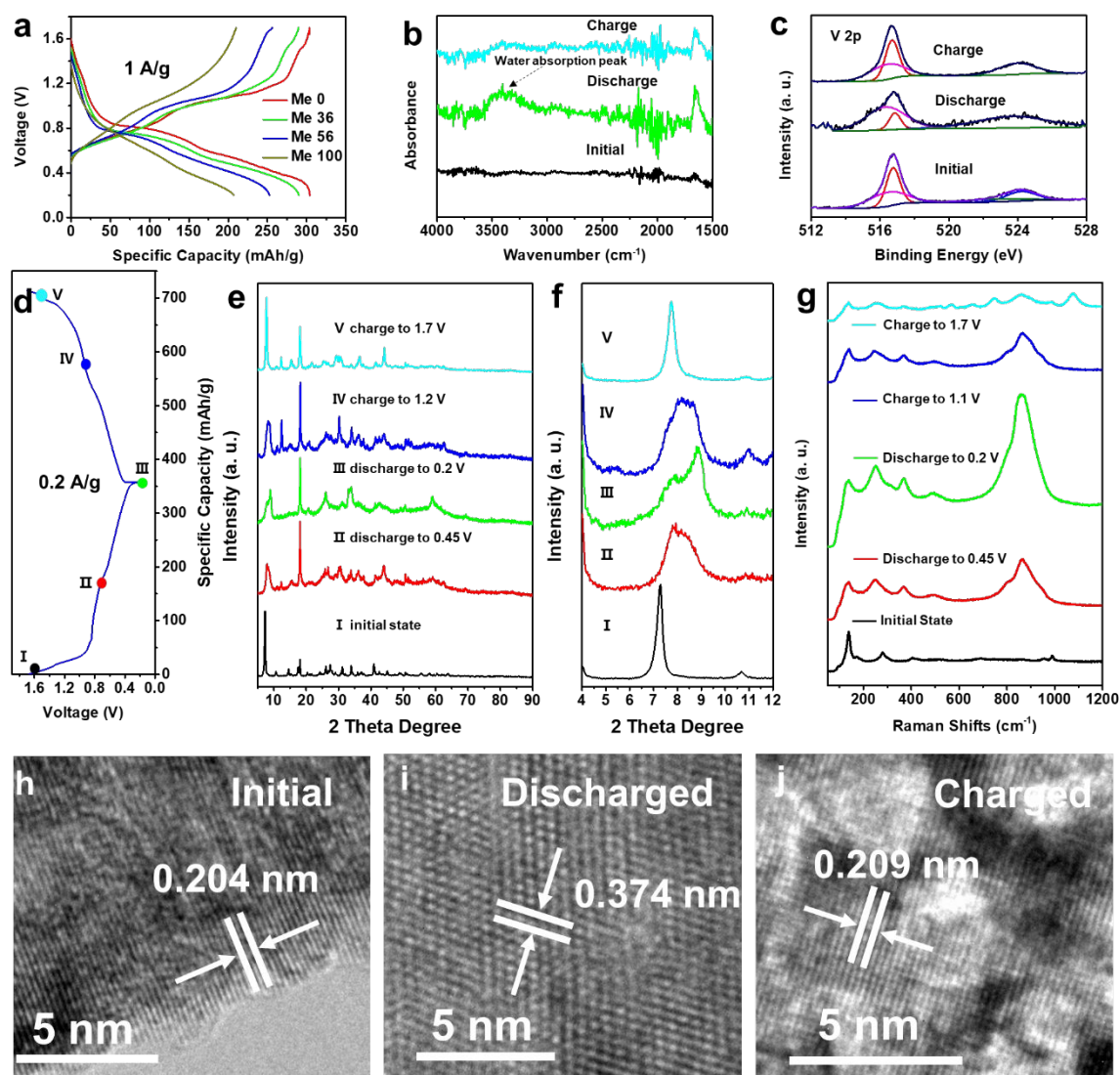


Figure 5. (a) Galvanostatic voltage-capacity profiles for MgVO/Zn batteries with different hybrid electrolyte at current density of 1 A/g. (b) FTIR (c) XPS spectra, (e-f) XRD results (g) Raman spectra (h-j) and HRTEM images of MgVO at different charge/discharge states (d) Galvanostatic voltage-capacity profile for ex-situ characterization.

5. Conclusions

Wood based CNF-polyacrylamide hydrogel was developed based on the Me56 hybrid electrolyte. The Me56 hybrid electrolyte shows the freezing point lower than -100 °C due to the strong hydrogen bonds between methanol molecule clusters with H₂O molecules. The reversibility of Zn anode is also boosted in this antisolvent since the Zn²⁺ solvation is weakened and corrosion reaction is suppressed. Based on the Me56 hybrid electrolyte, the developed CNF-PAM hydrogel electrolyte maintains its excellent mechanical properties at low temperatures, enabling the ssBs to be workable under repeated bending and twisting in very cold conditions. At the extremely low temperature of -60 °C, excellent electrochemical performance is also retained. This developed CNF-PAM hydrogel with hybrid electrolyte shows great potential to be applied in batteries for wearable devices at cold environment. The technology can also be potentially applied to build ssBs for extremely low temperature energy storages in remote areas.

Supporting Information

Supporting Information is available from the authors.

Acknowledgements

W. W. Xu and Chaozheng Liu contribute equally to this work. The authors acknowledge the financial support by USDA Forest Service/US Endowment (21-00157), Louisiana

Board of Regents [LEQSF(2020-23)-RD-B-02] and National Science Foundation (2120640).

Reference

1. T. Liu, X. Cheng, H. Yu, H. Zhu, N. Peng, R. Zheng, J. Zhang, M. Shui, Y. Cui and J. Shu, *Energy Storage Materials*, 2019, **18**, 68-91.
2. X. Dong, L. Chen, X. Su, Y. Wang and Y. Xia, *Angewandte Chemie International Edition*, 2016, **55**, 7474-7477.
3. G. Zhou, F. Li and H.-M. Cheng, *Energy & Environmental Science*, 2014, **7**, 1307-1338.
4. Q. Li, Q. Zhang, J. Sun, C. Liu, J. Guo, B. He, Z. Zhou, P. Man, C. Li and L. Xie, *Advanced Science*, 2019, **6**, 1801379.
5. H. Li, C. Han, Y. Huang, Y. Huang, M. Zhu, Z. Pei, Q. Xue, Z. Wang, Z. Liu and Z. Tang, *Energy & Environmental Science*, 2018, **11**, 941-951.
6. Q. Li, Q. Zhang, Z. Zhou, W. Gong, C. Liu, Y. Feng, G. Hong and Y. Yao, *Nano Research*, 2021, **14**, 91-99.
7. Q. Li, S. Jing, Z. Yong, Q. Zhang, C. Liu, K. Zhu, Y. Feng, W. Gong and Y. Yao, *Energy Storage Materials*, 2021, **42**, 815-825.
8. Q. Li, Q. Zhang, C. Liu, J. Sun, J. Guo, J. Zhang, Z. Zhou, B. He, Z. Pan and Y. Yao, *Journal of Materials Chemistry A*, 2019, **7**, 520-530.
9. Q. Li, Q. Zhang, C. Liu, W. Gong, Z. Zhou, P. Man, J. Guo, B. He, K. Zhang and W. Lu, *Energy Storage Materials*, 2020, **27**, 316-326.
10. D. Wang, H. Li, Z. Liu, Z. Tang, G. Liang, F. Mo, Q. Yang, L. Ma and C. Zhi, *Small*, 2018, **14**, 1803978.
11. S. Zhang, N. Yu, S. Zeng, S. Zhou, M. Chen, J. Di and Q. Li, *Journal of Materials Chemistry A*, 2018, **6**, 12237-12243.
12. Q. Li, *Small*, 2021, 2101617.
13. Q. Li, Q. Zhang, C. Liu, Z. Zhou, C. Li, B. He, P. Man, X. Wang and Y. Yao, *Journal of Materials Chemistry A*, 2019, **7**, 12997-13006.
14. W. Liu, M. S. Song, B. Kong and Y. Cui, *Advanced materials*, 2017, **29**, 1603436.
15. Y. Zeng, X. Zhang, Y. Meng, M. Yu, J. Yi, Y. Wu, X. Lu and Y. Tong, *Advanced Materials*, 2017, **29**, 1700274.
16. G. Fang, J. Zhou, A. Pan and S. Liang, *ACS Energy Letters*, 2018, **3**, 2480-2501.
17. F. Mo, G. Liang, Q. Meng, Z. Liu, H. Li, J. Fan and C. Zhi, *Energy & Environmental Science*, 2019, **12**, 706-715.
18. Q. Nian, J. Wang, S. Liu, T. Sun, S. Zheng, Y. Zhang, Z. Tao and J. Chen, *Angewandte Chemie*, 2019, **131**, 17150-17155.
19. N. Wang, X. Dong, B. Wang, Z. Guo, Z. Wang, R. Wang, X. Qiu and Y. Wang, *Angewandte Chemie*, 2020, **132**, 14685-14691.
20. Q. Zhang, Y. Ma, Y. Lu, L. Li, F. Wan, K. Zhang and J. Chen, *Nature communications*, 2020, **11**, 1-10.
21. D. W. McOwen, D. M. Seo, O. Borodin, J. Vatamanu, P. D. Boyle and W. A. Henderson, *Energy & Environmental Science*, 2014, **7**, 416-426.
22. J. Hao, L. Yuan, C. Ye, D. Chao, K. Davey, Z. Guo and S. Qiao, *Angewandte Chemie*.
23. N. Zhang, Z. Shen, C. Chen, G. He and C. Hao, *Journal of Molecular Liquids*, 2015, **203**, 90-97.
24. G. A. Miller and D. K. Carpenter, *Journal of Chemical & Engineering Data*, 1964, **9**, 371-373.

25. W. Yant, H. Schrenk and R. Sayers, *Industrial & Engineering Chemistry*, 1931, **23**, 551-555.
26. F. H. Conrad, E. Hill and E. Ballman, *Industrial & Engineering Chemistry*, 1940, **32**, 542-543.
27. U. Fałkowska, A. Radzka, A. Sławiński, A. Ryczkowski, M. Neścior and M. Tchórz, *Journal of Education, Health and Sport*, 2018, **8**, 996-1001.
28. M. Wang, L. Fan, G. Qin, X. Hu, Y. Wang, C. Wang, J. Yang and Q. Chen, *Journal of Membrane Science*, 2020, **597**, 117740.
29. J. Wang, F. Liu, F. Tao and Q. Pan, *ACS Applied Materials & Interfaces*, 2017, **9**, 27745-27753.
30. P. Yang, C. Feng, Y. Liu, T. Cheng, X. Yang, H. Liu, K. Liu and H. J. Fan, *Advanced Energy Materials*, 2020, 2002898.
31. W. Deng, Z. Zhou, Y. Li, M. Zhang, X. Yuan, J. Hu, Z. Li, C. Li and R. Li, *ACS nano*, 2020.
32. J. Zhang, M.-C. Li, X. Zhang, S. Ren, L. Dong, S. Lee, H. Cheng, T. Lei and Q. Wu, *Cellulose*, 2019, **26**, 4301-4312.
33. J. Zhang, Q. Wu, M.-C. Li, K. Song, X. Sun, S.-Y. Lee and T. Lei, *ACS Sustainable Chemistry & Engineering*, 2017, **5**, 7439-7447.
34. Y. Huang, M. Zhong, F. Shi, X. Liu, Z. Tang, Y. Wang, Y. Huang, H. Hou, X. Xie and C. Zhi, *Angewandte Chemie International Edition*, 2017, **56**, 9141-9145.
35. P. Xue, C. Guo, N. Wang, K. Zhu, S. Jing, S. Kong, X. Zhang, L. Li, H. Li and Y. Feng, *Advanced Functional Materials*, 2021, 2106417.
36. Y. Xu, X. Deng, Q. Li, G. Zhang, F. Xiong, S. Tan, Q. Wei, J. Lu, J. Li and Q. An, *Chem*, 2019, **5**, 1194-1209.
37. N. Zhang, F. Cheng, Y. Liu, Q. Zhao, K. Lei, C. Chen, X. Liu and J. Chen, *Journal of the American Chemical Society*, 2016, **138**, 12894-12901.
38. W. Xu, C. Liu, Q. Wu, W. Xie, W.-Y. Kim, S.-Y. Lee and J. Gwon, *Journal of Materials Chemistry A*, 2020, **8**, 18327-18337.
39. X. Zhang, J. Li, D. Liu, M. Liu, T. Zhou, K. Qi, L. Shi, Y. Zhu and Y. Qian, *Energy & Environmental Science*, 2021, **14**, 3120-3129.
40. S.-B. Wang, Q. Ran, R.-Q. Yao, H. Shi, Z. Wen, M. Zhao, X.-Y. Lang and Q. Jiang, *Nature communications*, 2020, **11**, 1-9.
41. G. Zhang, X. Zhang, H. Liu, J. Li, Y. Chen and H. Duan, *Advanced Energy Materials*, 2021, **11**, 2003927.
42. N. Chang, T. Li, R. Li, S. Wang, Y. Yin, H. Zhang and X. Li, *Energy & Environmental Science*, 2020, **13**, 3527-3535.
43. R. Vellacheri, A. Al-Haddad, H. Zhao, W. Wang, C. Wang and Y. Lei, *Nano Energy*, 2014, **8**, 231-237.
44. L. Su, L. Gong, H. Lü and Q. Xü, *Journal of Power Sources*, 2014, **248**, 212-217.
45. A. J. Roberts, A. F. D. De Namor and R. C. Slade, *Physical Chemistry Chemical Physics*, 2013, **15**, 3518-3526.
46. K. W. Nam, H. Kim, Y. Beldjoudi, T.-w. Kwon, D. J. Kim and J. F. Stoddart, *Journal of the American Chemical Society*, 2020, **142**, 2541-2548.
47. M. Yan, P. He, Y. Chen, S. Wang, Q. Wei, K. Zhao, X. Xu, Q. An, Y. Shuang and Y. Shao, *Advanced materials*, 2018, **30**, 1703725.
48. F. Ming, H. Liang, Y. Lei, S. Kandambeth, M. Eddaoudi and H. N. Alshareef, *ACS Energy Letters*, 2018, **3**, 2602-2609.
49. B. Sambandam, V. Soundharrajan, S. Kim, M. H. Alfaruqi, J. Jo, S. Kim, V. Mathew, Y.-k. Sun and J. Kim, *Journal of Materials Chemistry A*, 2018, **6**, 15530-15539.
50. F. Wan, L. Zhang, X. Dai, X. Wang, Z. Niu and J. Chen, *Nature communications*, 2018, **9**, 1656.

51. L. Shan, Y. Yang, W. Zhang, H. Chen, G. Fang, J. Zhou and S. Liang, *Energy Storage Materials*, 2019, **18**, 10-14.
52. P. Hu, T. Zhu, X. Wang, X. Zhou, X. Wei, X. Yao, W. Luo, C. Shi, K. A. Owusu and L. Zhou, *Nano Energy*, 2019, **58**, 492-498.
53. D. Kundu, B. D. Adams, V. Duffort, S. H. Vajargah and L. F. Nazar, *Nature Energy*, 2016, **1**, 1-8.
54. L. Wang, K.-W. Huang, J. Chen and J. Zheng, *Science advances*, 2019, **5**, eaax4279.
55. J. Shin, D. S. Choi, H. J. Lee, Y. Jung and J. W. Choi, *Advanced Energy Materials*, 2019, **9**, 1900083.